Analytical Aerodynamic Force and Moment Coefficients of Axisymmetric Objects in Rarefied Flow

Kenneth A. Hart,* Kyle R. Simonis,† Bradley A. Steinfeldt,‡ and Robert D. Braun§

Georgia Institute of Technology, Atlanta, GA, 30332-1510, USA

Recent developments in symbolic mathematics allow for analytic modeling of rarefied hypersonic aerodynamic coefficients of nontrivial geometries. These analytic models enable rapid trajectory propagation and sensitivity analysis for objects in low-Earth orbit. High fidelity modeling can be accomplished by generating an aerodynamic database via Direct Simulation Monte Carlo, however this process is computationally intractable considering the 13,000 pieces of debris in orbit. Analytic modeling provides a rapid alternative to DSMC with little loss of fidelity. In this investigation, the Schaaf & Chambré model is applied to geometries composed of conical frustums and cylindrical hulls, validated against DSMC results, and extended to arbitrary geometries of revolution with errors less than 5% relative to traditional numerical simulation.

Nomenclature

A	Area
C	Coefficient, see subscripts
Kn	Knudsen Number
l	Length
$\mathbf{n}$	Normal vector
R	Specific gas constant
r	Radius
s	Molecular speed ratio
T	Temperature
$\mathbf{t}$	Tangent vector
u	Parameterization variable
$\mathbf{V}$	Velocity
v	Parameterization variable

Subscripts

char	Characteristic
∞	Freestream
F	Force
M	Moment
N	Normal
p	Pressure
ref	Reference quantity
s	Shadowed
T	Tangential
τ	Shear
W	Wall

*Graduate Research Assistant, Daniel Guggenheim School of Aerospace Engineering, AIAA Student Member.
†Undergraduate Research Assistant, Daniel Guggenheim School of Aerospace Engineering, AIAA Student Member.
‡Research Engineer II, Daniel Guggenheim School of Aerospace Engineering, AIAA Member.
§David & Andrew Lewis Professor of Space Technology, Daniel Guggenheim School of Aerospace Engineering, AIAA Fellow.

w	Wetted

Symbols

α	Angle of attack
δ_c	Half cone angle
θ	Local freestream angle
λ	Mean free path, m
σ	Accommodation coefficient, see subscripts
Ω	Surface

I. Introduction

A. Motivation

As the number of objects in orbit about the Earth grows, the likelihood of any two of those objects colliding also increases. Tracking these objects and propagating their motion is an important aspect of space situational awareness,[1] though current models for propagating the influence of aerodynamics generally have poor geometric or physical fidelity. Inclusion of models of the aerodynamic forces and moments acting on the debris into trajectory propagation tools would benefit the characterization of objects in low Earth orbit (LEO).

Traditionally, rarefied aerodynamics are obtained through direct simulation Monte Carlo (DSMC), where a complex shape is gridded and paneled and the interaction with individual gas molecules is modeled.[2] In this investigation, an analytic method is developed that involves solving surface integrals; however, the analytic solutions can be evaluated much faster than a numerical simulation. The decrease in computation time associated with the analytic solutions enables rapid solution of the equations of motion for objects in LEO.

This investigation focuses on two general combinations of geometric primitives: the stepped cylinder and the biconic. Though these are not typical geometries for resident space objects (RSOs), they are the elemental bases for zeroth- and first-order approximations to surfaces of revolution. Extension of the stepped cylinder and biconic results to shapes with several cylinders or conical frustums can enable a lossless formulation for the rarefied aerodynamic coefficients of any arbitrary axisymmetric body. In this manner, verifying the analytic approach and results for these shapes is an important step in development of a general solution technique for the rapid computation of RSO aerodynamics.

B. Overview

In this investigation, analytic expressions for a stepped cylinder and a biconic geometry are derived. The work focuses primarily on the analytic raytracing required to define the mapping of shadows from one shape onto another. A key assumption in the derivation of these equations is that self-reflection of molecules in concave composite geometries is negligible compared to the effect of self-shadowing. There are often cases of self-reflection where the net effect is diminished because reflections from opposing surfaces negate each other. This sort of cancellation does not occur with the shadows of the surfaces, so it is reasonable to assume that self-shadowing is a greater effect than self-reflection. The analytic expressions are provided in the attachment embedded in the `pdf` version of this document and can be extracted from `AnalyticExpressions.pdf`.These expressions are compared in simulations against numerical results obtained by NASA-developed DSMC Analysis Code (DAC). The equations for the biconic are extended to approximate the Mars Microprobe aeroshell geometry,[3] demonstrating the application to arbitrary surfaces of revolution.

II. Background

In general, aerodynamic forces and moments arise from the momentum transferred from a fluid to an object submerged in that fluid. Fluid flows in a manner which conserves three fundamental quantities: mass, momentum, and energy.[4] All fluid flows are governed by the Boltzmann equation, which is a recasting of the three conservation laws and treats all fluids as a system of particles. The Boltzmann equation is more appropriate than the well-known Navier-Stokes equations in fluid flows about orbiting satellites due to the relatively low density of the fluid and high speeds required to maintain orbit. The regime of flows experienced

by RSOs is generally a rarefied flow, meaning that the density of molecules is so low that the gas no longer behaves like a continuum. Since Navier-Stokes only applies for continuum flows it cannot be applied in the rarefied regime and the Boltzmann equation governs the flow.

Traditionally, free-molecular flow theory is based upon the assumption that the flow incident on the body is independent of any effect of the particles reemitted from the surface of the body after collision.[5] Hence, the incident flow is entirely undisturbed by the presence of the body.[6] Though much of the literature rests on this assumption,[5–8] there have been investigations into cases where reemitted particles collide with the surface of the body more than once.[9,10] The similarity parameter that is generally used to define the interfaces between continuum flow, rarefied flow, and the regime between them known as transition flow, is the Knudsen Number (Kn) of the flow. This dimensionless quantity is defined in Eq. (1) as the ratio between the mean free path of the gas (λ) and the characteristic dimension (l_{char}) of the object submerged in the gas. So long as the Knudsen Number of a flow exceeds a value of 10, the flow regime is considered rarefied.[6] For reference, a 1U (10 cm $\times$ 10 cm $\times$ 10 cm) picosatellite will experience rarefied flows at altitudes above approximately 100 km on the Earth.[4]

$$\text{Kn} = \frac{\lambda}{l_{\text{char}}} \tag{1}$$

The accepted model for the coefficients of shear and pressure on a panel in rarefied flow are the Schaaf & Chambré model given by Eqs. (2) and (3).[6] The molecular speed ratio is defined in Eq. (4) as the ratio between the freestream velocity and the thermal velocity of the gas. In this equation, $||\cdot||$ is the Euclidean norm.

$$\begin{aligned} C_p = \frac{1}{s^2}\Bigg[&\left(\frac{2-\sigma_N}{\sqrt{\pi}} s\sin(\theta) + \frac{\sigma_N}{2}\sqrt{\frac{T_w}{T_\infty}}\right) e^{-(s\sin\theta)^2} \\ &+ \left\{(2-\sigma_N)\left((s\sin\theta)^2 + \frac{1}{2}\right) + \frac{\sigma_N}{2}\sqrt{\frac{\pi T_w}{T}} s\sin\theta\right\}(1+\text{erf}(s\sin\theta))\Bigg] \end{aligned} \tag{2}$$

$$C_\tau = -\frac{\sigma_T\cos\theta}{\sqrt{\pi}}\left[e^{-(s\sin\theta)^2} + \sqrt{\pi} s\sin\theta\,(1+\text{erf}(s\sin\theta))\right] \tag{3}$$

$$s = \frac{||\mathbf{V}_\infty||}{\sqrt{2RT_\infty}} \tag{4}$$

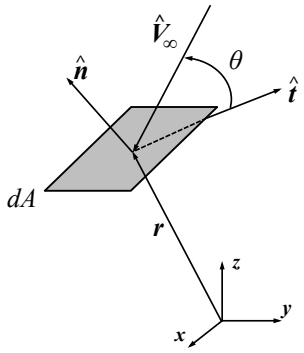

Figure 1. Diagram illustrating the relationships between relevant vector quantities.

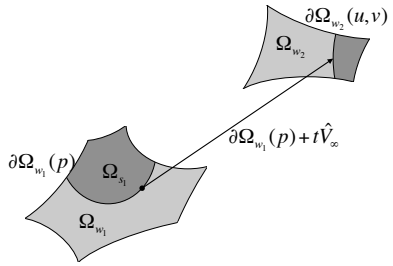

Figure 2. Map of the shadow from one surface onto another.

The pressure and shear coefficients for a flat plate derived by Schaaf & Chambré can be extended to curved surfaces by considering an infinitesimal element of area as shown in Figure 1. The normal and tangent vectors are scaled by the pressure and shear coefficients, respectively. This quantity, given in Eq. (5) describes the infinitesimal area's contribution to the overall aerodynamic force coefficients. In this equation, the $\hat{\cdot}$ over vector quantities indicate unit vectors. Crossing this elemental force contribution by the position of the element yields the elemental contribution to the moment coefficients as shown in Eq. (6). Integrating these infinitesimal quantities across the wetted region of the surface, defined by Eq. (7), results in the general integral definitions for aerodynamic force and moment coefficients given in Eqs. (8) and (9). The domain

of integeration defined in Eq. (7) is generally not the entire surface, Ω; it is the locus of points where the freestream velocity is above the local horizon.

$$d\mathbf{C}_F = \frac{1}{A_{\text{ref}}} \left(C_p \hat{\mathbf{n}} + C_\tau \hat{\mathbf{t}} \right) dA \tag{5}$$

$$d\mathbf{C}_M = \frac{1}{l_{\text{ref}}} \mathbf{r} \times d\mathbf{C}_F \tag{6}$$

$$\Omega_{\text{w}} := \{ \mathbf{r}(u,v) : \mathbf{V}_\infty \cdot \mathbf{n} \geq 0 \} \tag{7}$$

$$\mathbf{C}_F = \iint\limits_{\Omega_{\text{w}}} d\mathbf{C}_F \tag{8}$$

$$\mathbf{C}_M = \iint\limits_{\Omega_{\text{w}}} d\mathbf{C}_M \tag{9}$$

The normal and tangent vectors shown in Figure 1 can be computed from the parameterization of the surface. As shown in Eq. (10), the parameterization $\mathbf{r}$ maps the variables u and v onto the surface. So long as $\mathbf{r}$ is a regular parameterization, the normal vector $\hat{\mathbf{n}}$ is defined everywhere on Ω by Eq. (11). The angle of incidence, θ, between the tangent plane and the freestream vector is computed by Eq. (12). To define the tangent vector, as in Eq. (13), the normal component of the freestream vector is removed and the difference is normalized.

$$\mathbf{r} : (u,v) \to \Omega \tag{10}$$

$$\hat{\mathbf{n}} = \frac{\dfrac{\partial \mathbf{r}}{\partial u} \times \dfrac{\partial \mathbf{r}}{\partial v}}{\left\| \dfrac{\partial \mathbf{r}}{\partial u} \times \dfrac{\partial \mathbf{r}}{\partial v} \right\|} \tag{11}$$

$$\sin\theta = -\hat{\mathbf{V}}_\infty \cdot \hat{\mathbf{n}} \tag{12}$$

$$\hat{\mathbf{t}} = \frac{\hat{\mathbf{n}} \left(\hat{\mathbf{V}}_\infty \cdot \hat{\mathbf{n}} \right) - \hat{\mathbf{V}}_\infty}{\sqrt{1 - \left(\hat{\mathbf{V}}_\infty \cdot \hat{\mathbf{n}} \right)^2}} \tag{13}$$

These vector definitions and the rarefied aerodynamic models in Eqs. (2) and (3) fully define the general integral definitions for aerodynamic force and moment coefficients. The reference quantities A_{ref} and l_{ref} are constants of integration and serve to nondimensionalize the aerodynamic coefficients. The definitions given in Eqs. (5)-(7) and (10)-(13) provide explicit definitions for the aerodynamic force and moment integrals described in Eqs. (8) and (9). A more thorough derivation is available in the literature.[8]

For analytic geometries, this formulation provides exact aerodynamic characterization within the limits of the governing equations (Eqs. (2) and (3)), providing accurate sensitivity information and a rapid solution capability while eliminating the numerical error that is part of any numerical paneling tool. Calculation of aerodynamic properties in this manner eliminates the traditional use of large aerodynamic tables and enables use of fast, specialized trajectory optimization methods to be extended to also include vehicle sape. These techniques can also be used to instantaneously model configuration changes in flight due to breakup or atmospheric heating.

III. Methodology

A. Geometric Primitives

Analytic hypersonic rarefied aerodynamic coefficients have been previously investigated for the cone and the cylinder and show overall agreement with the results from DSMC.[5,7,8] The plots in Figure 3 show analytic curves validated against data points generated using DAC.

Analytic solutions for these primitive shapes that predict the aerodynamic coefficients can be obtained using the methodology outlined previously. This investigation explores applying that methodology to composite geometries and improving it so that arbitrary geometries of revolution can be modeled analytically.

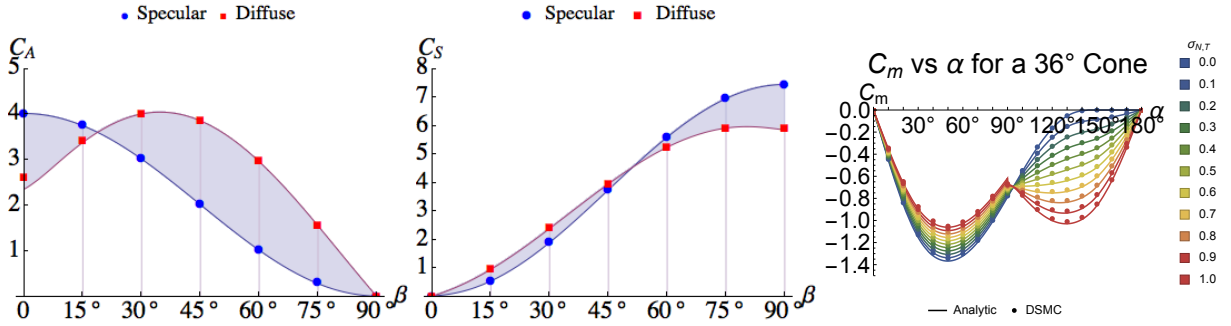

(a) Cylinder Axial Force Coefficient vs Sideslip Angle[8]

(b) Cylinder Side Force Coefficient vs Sideslip Angle[8]

(c) Cone Pitch Moment Coefficient vs Angle of Attack

Figure 3. Analytic curves and DAC data points for various geometric primitives.

B. Approximation of the Exponential and Error Functions

Applying the process defined in the previous section often results in integrals of the forms given by Eqs. (14) and (15). For most values of γ, these equations have no closed-form solution.

$$\int_0^{\gamma} \operatorname{erf}(s \sin\theta)\, d\theta \approx \gamma \tag{14}$$

$$\int_0^{\gamma} e^{-(s\sin\theta)^2}\, d\theta \approx 0 \tag{15}$$

To obtain a closed-form expression for the cone and the cylinder, the hyperthermal limit is applied in this investigation, where $\operatorname{erf} x \approx 1$ and $\exp -x^2 \approx 0$ for sufficiently large x. This limit has been applied in previous investigations, though self-shadowing was neglected in the derivations.[5,7] Over the majority of the surface of a cylindrical hull or conical frustum, the hyperthermal limit is a valid approximation; however, it breaks down at extremely low angles of incidence and for high-temperature gases.

C. Shadow Mapping

Piecewise surfaces which are locally convex but globally concave exhibit self-shadowing, where part of the surface could be invisible to the flow despite being oriented toward it. To map the shadow from one surface onto another, the locus of shadowed points on the first surface are transported along the freestream vector to the second surface. This defines a curve on the second surface which represents the boundary of the shadow. This process is illustrated in Figure 2. Which side of the curve the interior of the shadow maps to can be determined by testing a value within the shadow of the first surface and determining where it maps to on the second surface. The system of three equations in Eq. (16) has four unknowns: a coordinate, p, along $\partial\Omega_{w_1}$, the parameters u and v of Ω_2, and an arbitrary variable t that scales the freestream vector. These three equations, one for each entry in the position vector, are shown graphically in Figure 2 and mathematically in Eq. (16). From these three equations, a relationship between u and v on Ω_2 is derived to define the shadow boundary.

$$\partial\Omega_{w_2}(u,v) = \partial\Omega_{w_1}(p) + t\hat{\mathbf{V}}_{\infty} \tag{16}$$

D. Composition of the Stepped Cylinder

The stepped cylinder, shown in Figure 4(a), is geometrically defined by two non-intersecting coaxial cylinders joined at their planar surfaces. The geometry is axisymmetric, so the derivation of the aerodynamic coefficients assumes that the freestream velocity is in the x-z plane shown in Figure 4(a). This configuration has 5 parameterized surfaces: the forward panel, the forward cylindrical hull, the center panel, the aft cylindrical hull, and the aft panel. The parameterizations for these surfaces are given by Eqs. (17)-(21). It is assumed that the aft radius is greater than the forward radius for simplicity, since the converse can be handled by reversing the freestream direction.

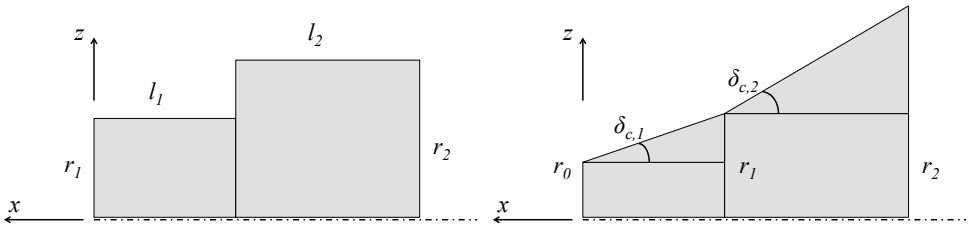

(a) Stepped Cylinder (b) Biconic

Figure 4. The stepped cylinder and biconic are two compositions of primitive geometries.

$$\mathbf{r}_{\text{forward panel}} = [0, \quad u_1 \sin v_1, \quad u_2 \cos v_1)]^\intercal \qquad u_1 \in [0, r_1], v_1 \in [-\pi, \pi] \tag{17}$$

$$\mathbf{r}_{\text{forward hull}} = [-u_2, \quad r_1 \sin v_2, \quad r_1 \cos v_2]^\intercal \qquad u_2 \in [0, l_1], v_2 \in [-\pi, \pi] \tag{18}$$

$$\mathbf{r}_{\text{middle panel}} = [-l_1, \quad u_3 \sin v_3, \quad u_3 \cos v_3]^\intercal \qquad u_3 \in [r_1, r_2], v_3 \in [-\pi, \pi] \tag{19}$$

$$\mathbf{r}_{\text{aft hull}} = [-l_1 - u_3, \quad r_2 \sin v_4, \quad r_2 \cos v_4]^\intercal \qquad u_4 \in [0, l_2], v_4 \in [-\pi, \pi] \tag{20}$$

$$\mathbf{r}_{\text{aft panel}} = [-l_1 - l_2, \quad v_5 \sin u_5, \quad v_5 \cos u_5]^\intercal \qquad u_5 \in [-\pi, \pi], v_5 \in [0, r_2] \tag{21}$$

1. Mapping from the Forward Cylinder to the Center Panel

The shadow on the center panel created by the forward cylinder is the shadow of a cylinder constrained by a circular boundary. The boundary of this shadow would be a complex piecewise function, however this is entirely unnecessary. Since the elemental forces are constant across a panel, it is sufficient to find the area of the shadow then subtract that area from the area of the center panel. Solving for this area is a matter of geometry, and the results are provided below.

$$A_w = \pi r_2^2 - \begin{cases} 2l_1 r_1 \tan(\alpha) + \pi r_1^2 & l_1 \tan(\alpha) \leq r_2 - r_1 \\ 2l_1 r_1 \tan(\alpha) + \pi r_1^2 & \\ \quad -2\Delta - r_1^2 \sec^{-1}\left(\dfrac{2l_1 r_1 \tan(\alpha)}{-l_1^2 \tan^2(\alpha) - r_1^2 + r_2^2}\right) & \\ \quad +r_2^2 \sec^{-1}\left(\dfrac{2l_1 r_2 \tan(\alpha)}{l_1^2 \tan^2(\alpha) - r_1^2 + r_2^2}\right) & r_2 - r_1 < l_1 \tan(\alpha) \leq \sqrt{r_2^2 - r_1^2} \\ \frac{\pi r_1^2}{2} + r_1\sqrt{r_2^2 - r_1^2} + r_2^2 \sin^{-1}\left(\frac{r_1}{r_2}\right) & \sqrt{r_2^2 - r_1^2} < l_1 \tan(\alpha) \end{cases} \tag{22}$$

$$\Delta = \frac{1}{4}\sqrt{(-l_1 \tan(\alpha) + r_1 + r_2)(l_1 \tan(\alpha) + r_1 - r_2)(l_1 \tan(\alpha) - r_1 + r_2)(l_1 \tan(\alpha) + r_1 + r_2)} \tag{23}$$

The complexity of this formula for the wetted area of the center panel is due to calculation of the lune between the edge of the panel and the edge of the shadow. In the case where the radii are significantly different in scale, then the second expression could be eliminated without a significant loss of fidelity. This would not be the case if the cylinders were approximations of a solid of revolution, so the lune area calculation is kept for completeness. Including the effect of self-shadowing from a cylinder onto a panel is accomplished by subtracting the area of the shadow from the total area of the panel.

2. Mapping from the Center Panel onto the Forward Cylinder

When the freestream velocity forms an obtuse angle with the x-axis, the center panel shadows the forward cylinder. Unlike the previous case, the boundary of this shadow can be determined in a straightforward, analytic raytracing process. The first step in this process is to parameterize the edge of the shadow. This boundary is a circle given by Eq. (25).

$$\partial\Omega_{w_3} = \mathbf{r}_{\text{middle panel}}\big|_{u_3 = r_2} \tag{24}$$

$$\partial\Omega_{w_3} = [-l_1, \quad r_2 \sin v_3, \quad r_2 \cos v_3]^\intercal \tag{25}$$

Mapping this boundary to the forward shadow using Eq. (16) results in the system of equations in Eqs. (26)-(28). This system can be used to isolate u_2 and v_2 and describe the shadow on the forward hull caused by the aft hull. This relationship between u_2 and v_2 is given by Eq. (29).

$$u_2 = l_1 + t\cos\alpha \tag{26}$$

$$r_1 \sin v_2 = r_2 \sin v_3 \tag{27}$$

$$r_1 \cos v_2 = r_2 \cos v_3 - t\sin\alpha \tag{28}$$

$$u_2(v_2) = l_1 - \cot\alpha\left(\sqrt{r_2^2 - r_1^2\sin^2 v_2} + r_1\cos v_2\right) \tag{29}$$

The effect of self-shadowing can be incorporated by considering Eq. (29) to be a limit of integration in u. Unfortunately, after the u-integration of Eqs. (8) and (9), the v-integrals do not have closed-form solutions. Another issue with this definition of the shadow boundary arise when the shadow boundary intersects the natural bound on the cylinder. These issues are overcome by considering the extreme value of u on the shadow and eliminating the dependence on v. Substituting $\pi/2$ for v yields the result in Eq. (30). This approximation is also advantageous because the wetted area of the forward surface is approximated by a shorter cylindrical hull, a surface for which closed-form expressions have been previously derived and validated.

$$u_2(v_2) \approx u_2\left(\frac{\pi}{2}\right) = l_1 + \cot\alpha\sqrt{r_2^2 - r_1^2} \tag{30}$$

E. Composition of the Biconic

The biconic geometry, shown in Figure 4(b), is defined in this investigation as a conical frustum that is followed by a second frustum. The parameterizations for each distinct surface on the biconic are given by Eqs. (32)-(38). Whether the cone angle of the aft frustum is greater than or less than that of the forward frustum will result in different shadow mappings. In the case where the cone angle increases, the forward frustum casts a shadow onto the aft frustum and reflects air molecules onto it. For a decreasing cone angle, the two frustums can be superimposed without loss of fidelity because self-reflection cannot occur and the shadow from the first frustum is entirely contained within the shadow of the aft frustum.

$$\mathbf{r}_{\text{forward panel}} = [0, \quad u_1\sin v_1, \quad u_2\cos v_1)]^\intercal \tag{31}$$

$$u_1 \in [0, r_0], v_1 \in [-\pi, \pi] \tag{32}$$

$$\mathbf{r}_{\text{forward frustum}} = [r_0\cot\delta_{c_1} - u_2, \quad u_2\tan\delta_{c_1}\sin v_2, \quad u_2\tan\delta_{c_1}\cos v_2]^\intercal \tag{33}$$

$$u_2 \in [r_0\cot\delta_{c_1}, r_1\cot\delta_{c_1}], v_2 \in [-\pi, \pi] \tag{34}$$

$$\mathbf{r}_{\text{aft frustum}} = [r_1\cot\delta_{c_2} - (r_1 - r_0)\cot\delta_{c_1} - u_3, \quad u_3\tan\delta_{c_2}\sin v_3, \quad u_3\tan\delta_{c_2}\cos v_3]^\intercal \tag{35}$$

$$u_3 \in [r_1\cot\delta_{c_2}, r_2\cot\delta_{c_2}], v_3 \in [-\pi, \pi] \tag{36}$$

$$\mathbf{r}_{\text{aft panel}} = [-(r_1 - r_0)\cot\delta_{c_1} - (r_2 - r_1)\cot\delta_{c_2}, \quad v_4\sin u_4, \quad v_4\cos u_4]^\intercal \tag{37}$$

$$u_4 \in [-\pi, \pi], v_4 \in [0, r_2] \tag{38}$$

For biconic geometries the integration across the forward conical frustum is the same, while the aft frustum integration varies. The forward conical frustum naturally shadows itself whenever the freestream angle is greater than its cone angle. This condition is given by Eq. (39), where the real function, Re, is used to eliminate the need for a conditional or piecewise function in the limits of integration. When the cone angle is greater than the freestream angle, the real part of the arccosine is identically π, so the limits of integration would be $-\pi$ and π. With the domain of integration defined by the shadow boundary, closed-form expressions for the aerodynamic coefficients of the forward conical frustum can be calculated.

$$v_2 = \pm\text{Re}\left(\cos^{-1}\left(-\cot(\alpha)\tan\left(\delta_{c_1}\right)\right)\right) \tag{39}$$

1. Increasing Biconic

In this biconic configuration, the forward frustum shadows onto the aft frustum when the freestream angle is greater than the cone angle of the forward cone. Applying the analytic raytracing technique from Eq. (16), the shadow on the aft cone is given by Eq. (40).

$$u_3 = \frac{\cot\left(\delta_{c_2}\right)\left(\cot\left(\delta_{c_2}\right) - \cot\left(\delta_{c_1}\right)\right)\left(r_0 \cot\left(\delta_{c_1}\right) + l_1\right)\eta}{\cot\left(\delta_{c_2}\right)\cot\left(\delta_{c_1}\right)\eta - \sin(v_3)\cot^2\left(\delta_{c_1}\right) + \cot(\alpha)\cos(v_3)\cot\left(\delta_{c_1}\right)\eta + \cot^2(\alpha)\sin(v_3)} \tag{40}$$

$$\eta = \sqrt{1 - \cot^2(\alpha)\tan^2\left(\delta_{c_1}\right)} \tag{41}$$

The boundary of the shadow given by Eq. (40) describes a hyperbola. The shadow boundary on the forward conical frustum is linear and the normal vector along that boundary is constant, so there is a tangent plane along this shadow boundary. This plane intersects the aft conical frustum, generating a conic section, and due to the geometry of this problem that section is a hyperbola. This hyperbolic bound can be introduced into the u limits of integration, however the resulting v integral cannot be evaluated closed-form. To solve this problem, the parameter from Eq. (39) for the front frustum is used as the shadow boundary of the aft frustum. Geometrically, this approximation is significantly different from the exact hyperbolic solution in Eq. (40), however the area between the these two boundaries does not contribute significantly to the overall aerodynamic coefficients. Since the u-integration is unchanged under the asymptote approximation and the v-integration bounds are constants, the aerodynamic coefficients for the aft frustum can be derived in closed-form.

2. Decreasing Biconic

The case of the decreasing biconic, where the aft cone angle is less than the forward cone angle, is more straightforward because two conical frustums can be superimposed without loss of fidelity in the model or geometry. The shadow from the forward frustum can be mapped onto the aft frustum using the analytic raytracing method and the result is that the mapped shadow is always contained within the natural shadow of the aft frustum. In this case, no hyperbolic approximation is necessary; the integration process for the aft frustum is identical to the process for the forward frustum. This result can be applied directly to any solid of revolution whose radius function has a monotonically decreasing slope. Geometries including paraboloids, oblate spheroids, ogives, and sphere-cones can all be discretized and summed by the trapezium formula to yield their aerodynamic coefficients.[11]

F. Arbitrary Axisymmetric Geometry

The methodology above for combining two shape primitives can be extended to any number of primitives to approximate an arbitrary axisymmetric geometry. For such shapes, the radius at a point on shape is a function of its axial position. Approximating this function with piecewise-constant values yields a stepped cylinder geometry. Using a piecewise-linear approximation to the radius function would yield a surface composed of conical frustums. Consider a surface of revolution defined by Eq. (42). The function f can be sampled at a list of u values, and between the samplings the function is approximately linear as shown in Eq. (43). Since the integral is a linear operator, the equations for the force and moment coefficients can be evaluated on the ith interval and summed to obtain an expression for entire surface.

$$\mathbf{r} = [u, f(u)\sin v_1, \quad f(u)\cos v_1)]^\intercal \tag{42}$$

$$f(u) \approx \begin{cases} f_1 + \frac{u-u_1}{u_2-u_1}(f_2 - f_1) & u_1 \le u < u_2 \\ f_2 + \frac{u-u_2}{u_3-u_2}(f_3 - f_2) & u_2 \le u < u_3 \\ \dots & \dots \\ f_i + \frac{u-u_i}{u_{i+1}-u_i}(f_{i+1} - f_i) & u_i \le u < u_i + 1 \\ \dots & \dots \\ f_{n-1} + \frac{u-u_{n-1}}{u_n-u_{n-1}}(f_n - f_{n-1}) & u_{n-1} \le u < u_n \end{cases} \tag{43}$$

The assumptions made in generating the biconic and stepped cylinder equations tend to break down when there is a significant variation in the properties of each element. This approximation is appropriate for radius functions that are piecewise smooth and have a continuous derivative. More specifically, if the radius function has a monotonically decreasing derivative, then approximating the surface with a series of conical frustums will produce aerodynamic coefficients without a loss of model fidelity.

IV. Results

To illustrate the application of this composition methodology, the analytic aerodynamic coefficients for the shapes in Figure 5 were compared against DAC simulation data. The first three shapes are the elemental compositions, the stepped cylinder and the two biconics, and the fourth is the aeroshell of Mars Microprobe approximated by a series of conical frustums. The results for each of these composite geometries compare favorably with the results from DAC simulations in terms of both accuracy and speed. For each of these shapes, the reference area is the base area, the reference length is the total length, and the moments are taken about the nose.

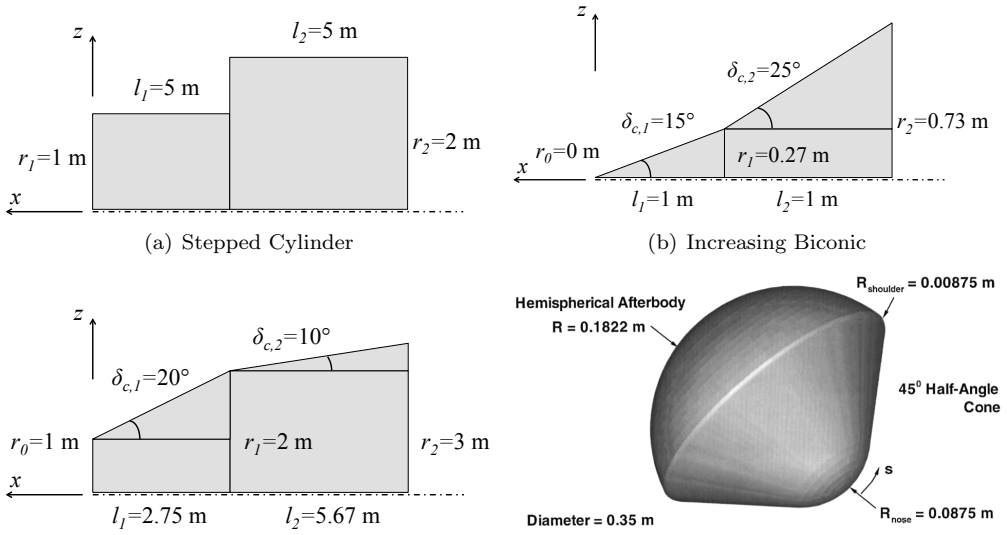

(a) Stepped Cylinder

(b) Increasing Biconic

(c) Decreasing Biconic

(d) Mars Microprobe Aeroshell[3]

Figure 5. Validation geometries for analytic aerodynamic coefficients.

A. Stepped Cylinder

An aerodynamic database for the stepped cylinder shown in Figure 5(a) was generated using the analytic models and compared against DAC simulations. The plots in Figure 6 show consistent agreement between the analytic model and DAC results. The model does not include self-reflection of molecules, a feature that is apparent in the axial force coefficient at angles of attack of $10° - 20°$. The difference between the analytic and numerical results is more significant for specular reflections. This effect is not apparent for diffuse molecular reflections, which is more common in nature. For diffuse reflections, self-shadowing is a more significant effect than self-reflection and the two models consistently predict the same values for the aerodynamic coefficients within a 5% difference.

B. Increasing Biconic

For the increasing biconic geometry shown in Figure 5(b), there is consistent matching of the DAC and analytic predictions in the case of diffuse reflections. In Figure 7, the effects of self-reflection are evident in the error plots at 20°, 150°, and 160°. The magnitude of the error decreases as the accommodation coefficient increases. For diffuse reflections, the analytic and DAC results are within 5% difference. The analytic model also accurately predicts the angles of attack where the coefficients become invariant to the accommodation coefficient, best illustrated in the axial force coefficient plot.

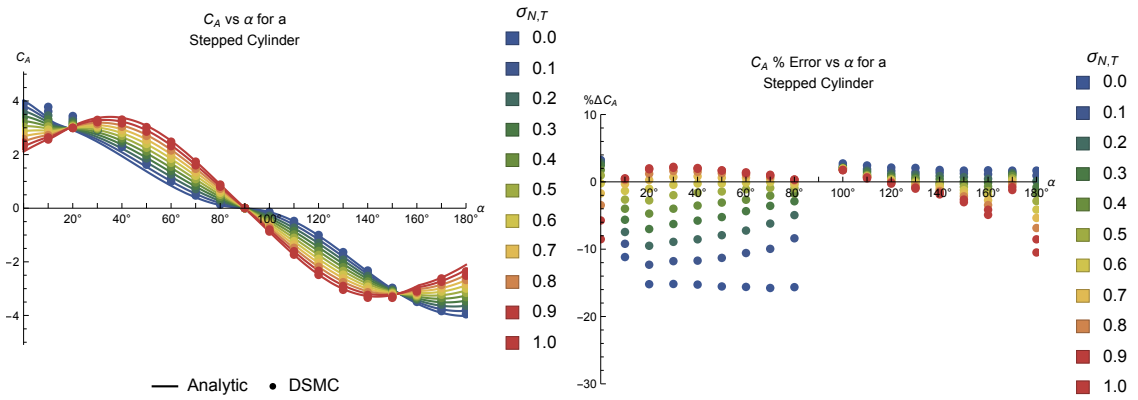

(a) Axial Force Coefficient

(b) Axial Force Coefficient Percent Error

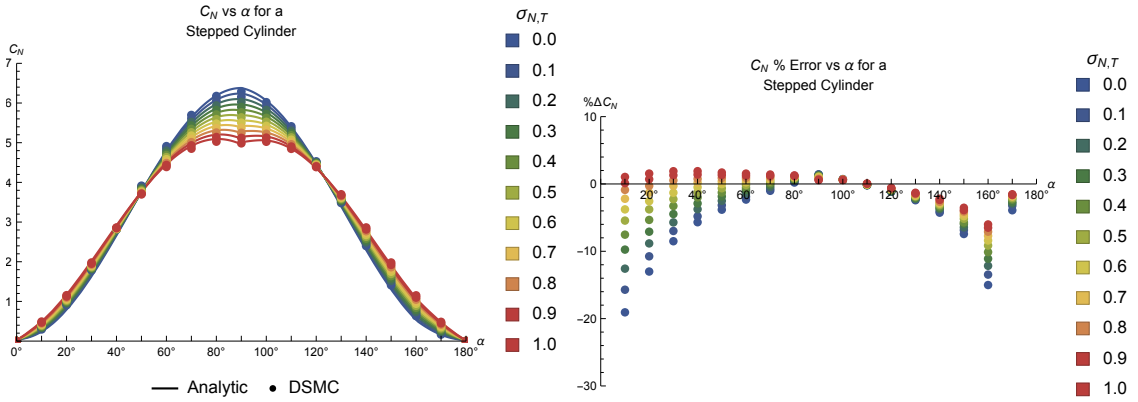

(c) Normal Force Coefficient

(d) Normal Force Coefficient Percent Error

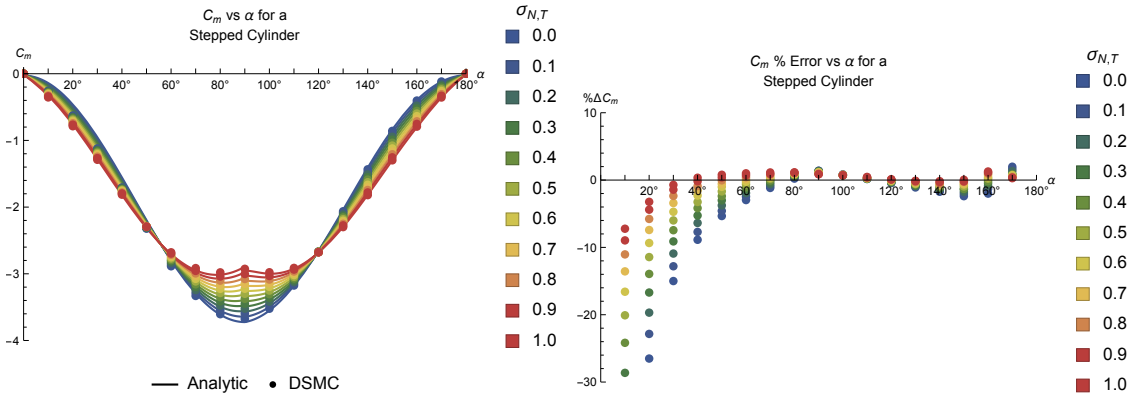

(e) Pitch Moment Coefficient

(f) Pitch Moment Coefficient Percent Error

Figure 6. Comparison of Analytic and DAC estimates of the rarefied aerodynamic coefficients of a stepped cylinder.

C. Decreasing Biconic

Strong agreement between the analytic and DAC results is shown in Figure 8 for the decreasing biconic geometry. The geometry detailed in Figure 5(c) was analyzed as a representative example. At all angle of attacks and accommodation coefficients, the analytic equations predict aerodynamic coefficients that are consistent with the DAC simulations up to 5%. Of the three elemental superpositions of geometric primitives, the decreasing biconic is the most promising candidate for the basis of modeling an arbitrary surface of revolution.

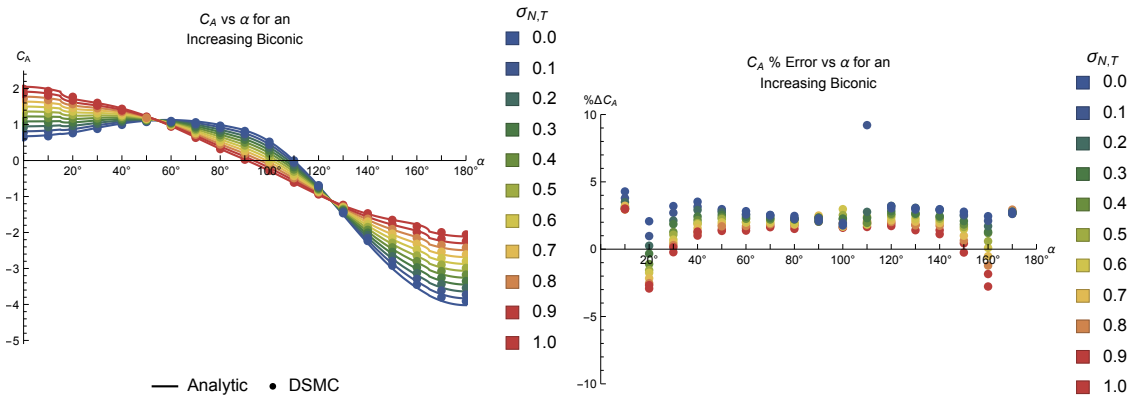

(a) Axial Force Coefficient

(b) Axial Force Coefficient Percent Error

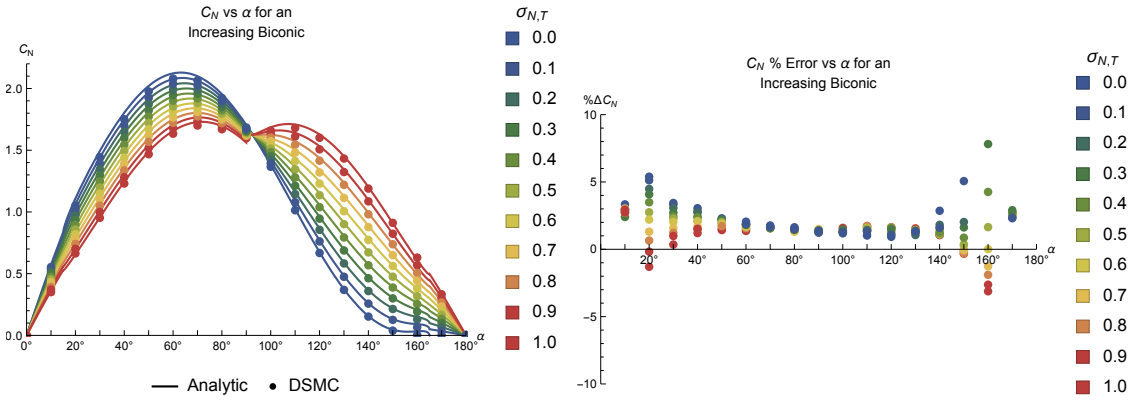

(c) Normal Force Coefficient

(d) Normal Force Coefficient Percent Error

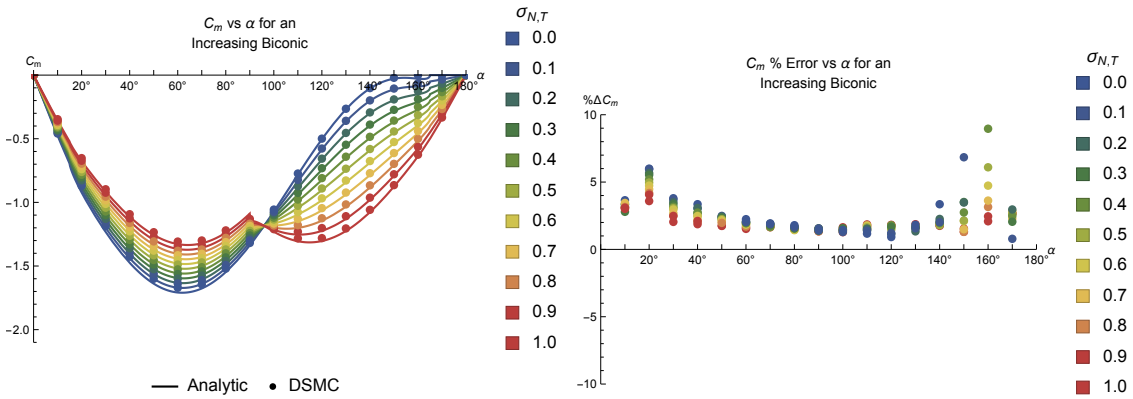

(e) Pitch Moment Coefficient

(f) Pitch Moment Coefficient Percent Error

Figure 7. Analytic and DAC estimates for the aerodynamic coefficients of an increasing biconic.

D. Arbitrary Surface of Revolution

The formulation for the arbitrary surface of revolution is applied to the Mars Microprobe aeroshell, shown in Figure 5(d). The analytic model is compared in Figure 9 against published DSMC results.[3]

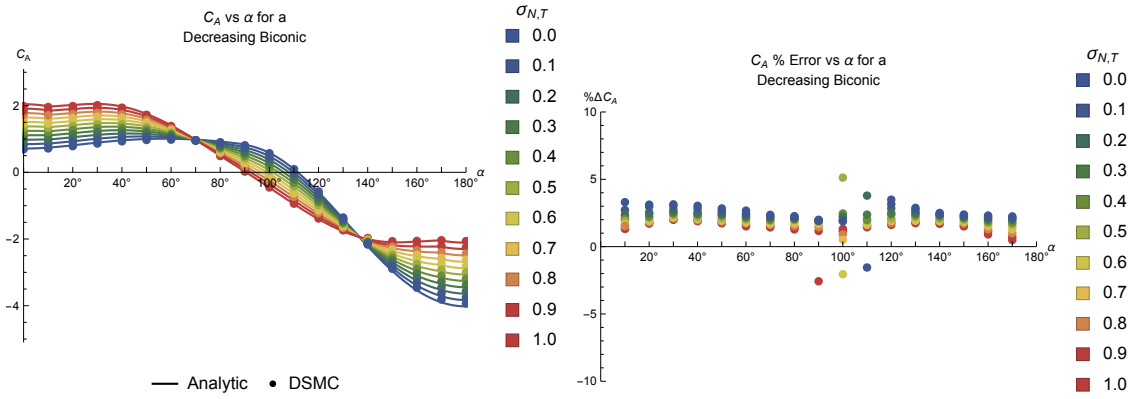

(a) Axial Force Coefficient

(b) Axial Force Coefficient Percent Error

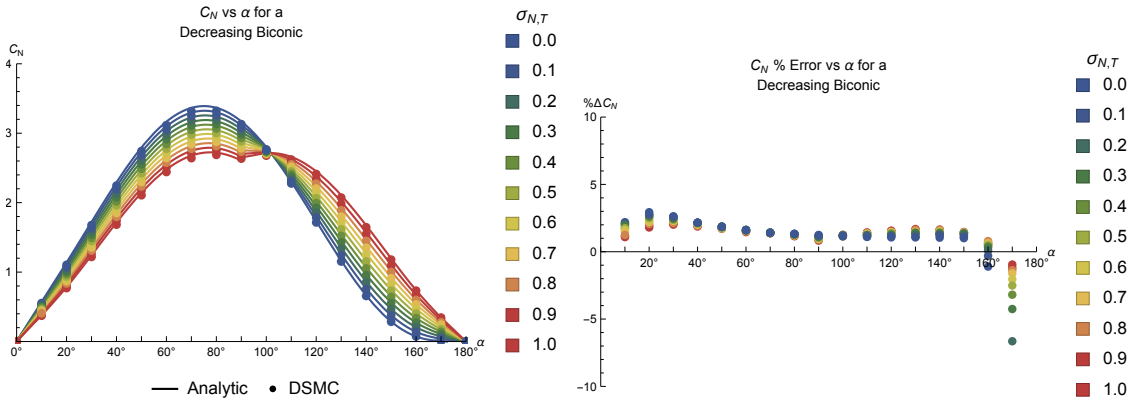

(c) Normal Force Coefficient

(d) Normal Force Coefficient Percent Error

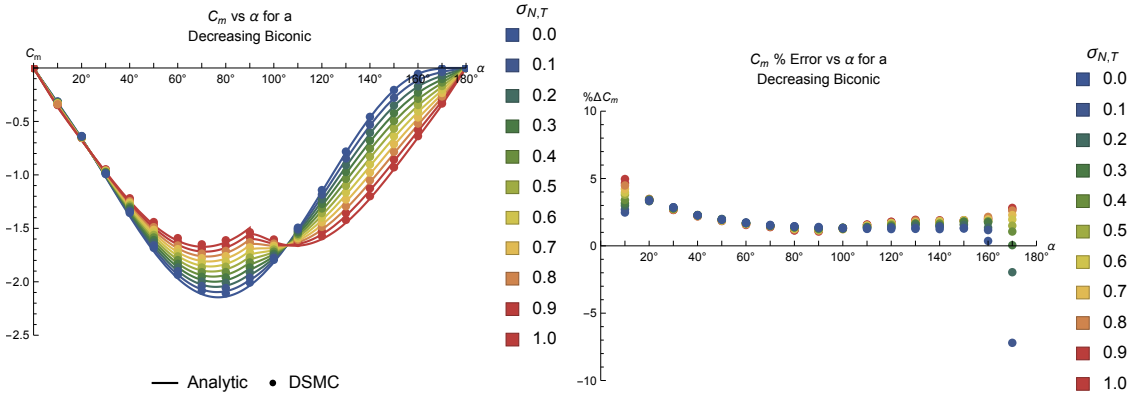

(e) Pitch Moment Coefficient

(f) Pitch Moment Coefficient Percent Error

Figure 8. Aerodynamic coefficients of a decreasing biconic as predicted by the analytic solution and DAC.

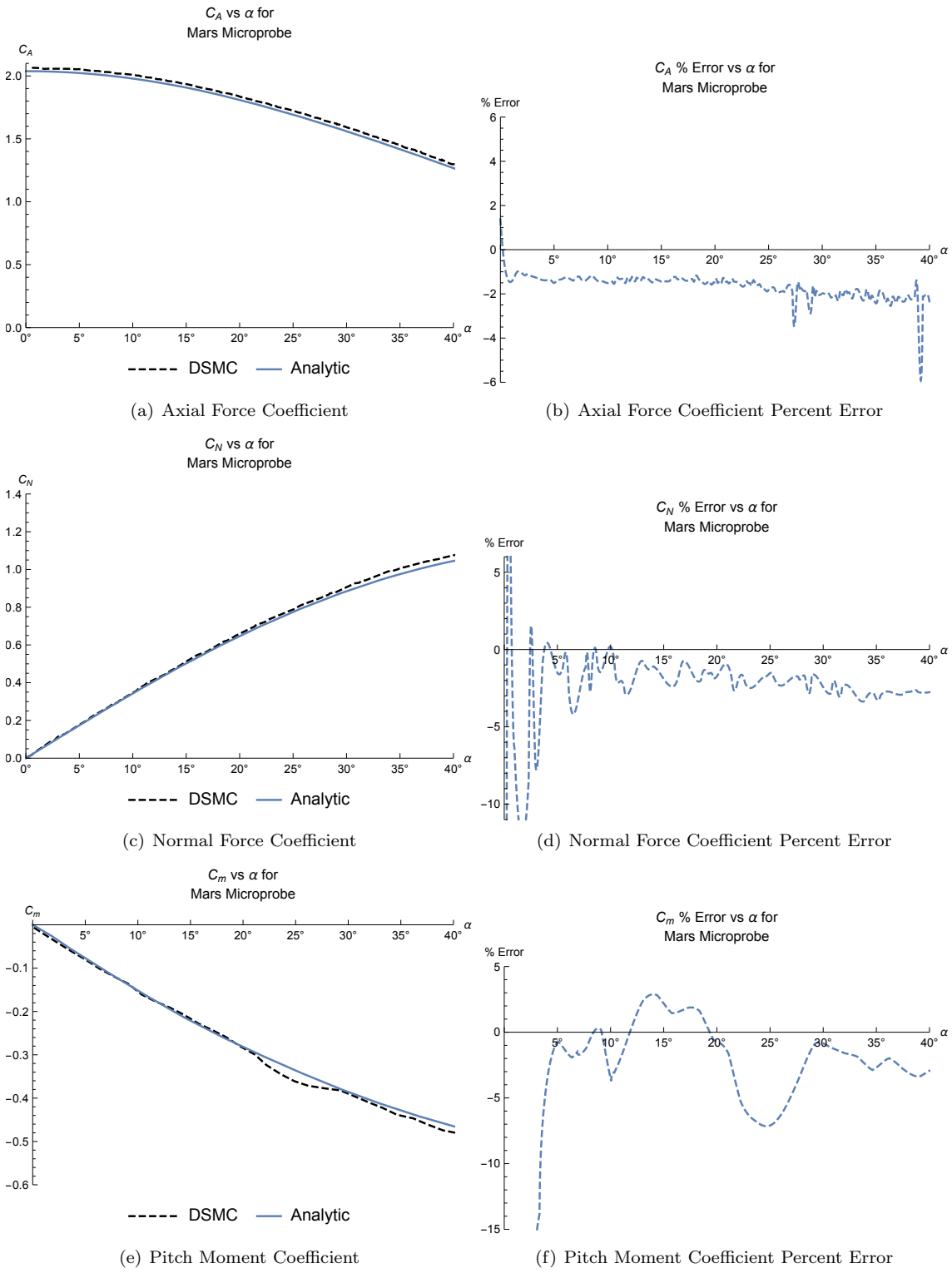

(a) Axial Force Coefficient

(b) Axial Force Coefficient Percent Error

(c) Normal Force Coefficient

(d) Normal Force Coefficient Percent Error

(e) Pitch Moment Coefficient

(f) Pitch Moment Coefficient Percent Error

Figure 9. Analytic and DSMC curves for the rarefied aerodynamics of the Mars Microprobe aeroshell.[3]

The conical frustum approximation to the aeroshell geometry will yield lengthy equations for each of these aerodynamic coefficients; however, the evaluation process is significantly faster than DSMC. Sampling the angle of attack range from 0 to 40 degrees took less time to evaluate analytically than a single DAC run takes. Approximating surfaces of revolution by a series of conical frustums yields aerodynamic coefficients similar to DSMC generated coefficients with a significant reduction in computation time, shown in Table 1. These runtimes were taken from a computer with an 2.8 GHz Intel Core 2 Duo processor and 4 GB of memory. The analytic formulation also enables computation of stability derivatives and rapid trajectory propagation.

Table 1. Runtime comparison for computing rarefied aerodynamics.

Method	Runtime
Analytic	57 ms
DSMC	11 min

V. Summary

Analytic rarefied aerodynamic coefficients are derived for the stepped cylinder and the biconic geometries. To map the shadows from one surface to another, an analytic raytracing methodology is developed and applied in the derivation of the aerodynamic coefficients. The resulting equations compare well with numerical simulations, within the limits of the governing equations. Extension of the biconic coefficients to an arbitrary surface of revolution also matches with numerical simulations, at a significantly shorter computation time.

Future work in analytic modeling of rarefied aerodynamic coefficients would focus on more complicated geometries and improvement on the elemental force model to capture self-reflection. More advanced geometries could include ellipse cones and, more generally, geometries with varying elliptical cross sections. The equation for the conical frustum element of an arbitrary surface of revolution is derived with a finite interval width. Taking the limit as this width goes to zero would yield the integrands for force and moment coefficients of arbitrary surfaces of revolution without the piecewise linear approximation. The elemental force model currently considers a single freestream velocity; however, there can be multiple sources of particles in a concave shape. This could be modeled by developing view factors for each surface or possibly by considering the tangent vector to be distributed probabilistically on the tangent plane.

Acknowledgments

The work in this paper was funded by Air Force Research Laboratory Contract No. FA9453-13-C-0205.

References

[1]Liou, J.-C., NASA, NASA Orbital Debris Program Office, and Lious, J.-C., "Orbital Debris Quarterly News," Tech. rep., National Aeronautics and Space Administration, Houston, TX, Jan. 2014.

[2]LeBeau, G. J. and Lumpkin III, F. E., "Application highlights of the DSMC Analysis Code (DAC) software for simulating rarefied flows," *Computer Methods in Applied Mechanics and Engineering*, Vol. 191, 2001, pp. 595–609.

[3]Mitcheltree, R. A., Moss, J. N., Cheatwood, F. M., Greene, F. A., and Braun, R. D., "Aerodynamics of the Mars Microprobe Entry Vehicles," *Journal of Spacecraft and Rockets*, Vol. 36, No. 3, May 1999, pp. 392–398.

[4]Regan, F. J. and Anandakrishnan, S. M., *Dynamics of Atmospheric Re-Entry*, American Institute of Aeronautics and Astronautics, Reston, VA, 1993.

[5]Sentman, L. H., "Free Molecular Flow Theory and its Application to the Determination of Aerodynamic Forces," Tech. rep., 1961.

[6]Schaaf, S. A. and Chambre, P. L., *Flow of Rarefied Gases*, Princeton University Press, 1961.

[7]Stalder, J. R. and Zurick, V. J., "Theoretical Aerodynamic Characteristics of Bodies in a Free-Molecule-Flow Field," Tech. rep., 1951.

[8]Hart, K. A., Dutta, S., Simonis, K. R., Steinfeldt, B. A., and Braun, R. D., "Analytically-derived Aerodynamic Force and Moment Coefficients of Resident Space Objects in Free-Molecular Flow," *AIAA Atmospheric Flight Mechanics Conference, National Harbor, MD*, Jan. 2014.

[9]Pratt, M. J., "Concave surfaces in free molecule flow," *AIAA Journal*, Vol. 1, No. 7, 1963, pp. 1716–1717.

[10]Schamberg, R., "On Concave Bodies in Free Molecule Flow," 1967.

[11]Hildebrand, F. B., *Introduction to numerical analysis*, Courier Dover Publications, 1987.